View metadata, citation and similar papers at core.ac.uk

brought to you by CORE

provided by NASA Technical Reports Server

IN-46-CR
85773

Semiannual Status Report

NASA-Ames Cooperative Agreement Number NCC 2-662

P.27

MODELLING ATMOSPHERIC SCATTERERS USING SPACECRAFT OBSERVATIONS

For the period October 1, 1991 through March 31, 1992

Submitted to

Dr. James B. Pollack, Technical Officer
Theoretical Studies Branch, 245-3
National Aeronautics and Space Administration
Ames Research Center
Moffett Field, California 94035

Prepared by

Dr. Kathy A. Rages, Principal Investigator
Space Physics Research Institute
572 Hyannis Drive
Sunnyvale, California 94087-1315
(408) 736-9705

(NASA-CR-190263) MODELLING ATMOSPHERIC SCATTERERS USING SPACECRAFT OBSERVATIONS Semiannual Status Report, 1 Oct. 1991 - 31 Mar. 1992 (Space Physics Research Inst.) 27 p

N92-25369

CSCL 04A G3/46

Unclas
0085773

Progress Report

Work this period focussed on the preparation of the manuscript " Voyager Imaging of Triton's Clouds and Hazes" (Appendix A) which has been submitted to Icarus.

Appendix A

VOYAGER IMAGING OF TRITON'S CLOUDS AND HAZES

Kathy Rages
Space Physics Research Institute
Sunnyvale, California 94087
(415) 604-6735
Internet Address: rages@gal.arc.nasa.gov

James B. Pollack
Space Science Division
NASA Ames Research Center
Moffett Field, California 94035
(415) 604-5530

Tuesday, March 31, 1992

19Pages
4 Tables
6 Figures

Abstract

Voyager images of Triton indicate considerable spatial variability in the concentration of at least two different scattering components in the atmosphere. Data from high phase angle limb scans have been fit to Mie scattering models to derive mean particle sizes, number densities, and vertical extent for both types of scattering material at ten different locations between 15°S and 70°S. These fits reveal a thin haze at latitudes equatorward of 25-30°S. The imaging data can be fit reasonably well by both conservatively scattering and absorbing hazes with particle sizes near 0.18 μm and optical depths of order 0.001-0.01. Rayleigh scattering haze fits the imaging data somewhat less well, and can be totally ruled out by combining the imaging and UVS measurements. At high southern latitudes, Triton displays clouds below an altitude of ~8 km, as well as the haze at higher altitudes. The clouds have particle sizes which may range from 0.7-2.0 μm, or may be near 0.25 μm. The atmospheric optical depth poleward of 30°S must be generally greater than 0.1, but need not be more than 0.3. Horizontal inhomogeneities are quite noticeable, especially at longitudes east of (i.e. higher than) 180°.

1. Introduction

Until the Voyager encounter with Neptune very little was known about its largest satellite Triton. Even estimates of Triton's radius were uncertain. It was known from measurements of the infrared spectrum (Cruikshank *et al.* 1984, Cruikshank *et al.* 1989) that condensed nitrogen was present in some form on the surface, but the surface pressure and temperature and the atmospheric optical depth were unknown. From radio occultation data taken during the Voyager encounter (Tyler *et al.* 1989) it was determined that Triton possessed an atmosphere which was mostly nitrogen, with a surface pressure of about 12 μbar and a surface temperature of 37K. Despite this exceedingly low pressure, images of Triton's limb taken near closest approach clearly show some kind of scattering layer above the surface (Smith *et al.* 1989). A detailed analysis of these images (Pollack *et al.* 1990) indicated that a thin haze, presumeably of photochemical origin, is present nearly everywhere on Triton. In addition, a sizable fraction of the surface poleward of 30°S is covered by discrete clouds which are confined to the lower 8 km of the atmosphere and may have optical depths of order 0.1. The confinement of these clouds to the lower part of Triton's atmosphere and high southern latitudes suggests that they are composed of nitrogen ice.

In this paper, we will present the results of a detailed analysis of the Voyager images of Triton taken at the highest solar phase angles. Although the spatial resolution of these images is lower than that of the images studied in Pollack *et al.* (1990), observations at high phase angles are more sensitive to properties such as the particle sizes and vertical extinction profiles of the hazes and clouds than the highest resolution images were. In the next section, we outline our data analysis procedure. In sections 3 and 4 we discuss the properties of atmospheric models derived for low and high southern latitudes, respectively. Section 5 contains a more detailed discussion of localized atmospheric features, and the final section considers some implications of our findings for models of seasonal changes on Triton.

2. Data set

The data set consists of fifteen Voyager wide angle images of Triton taken at high solar phase angles (140°–160°). Three of these images were taken with the violet filter, five with the blue filter, five with the green filter, and two with the orange filter. The linear resolution in these images ranged from about 10 kilometers per line pair (km/lp) at the beginning of the sequence (highest phase angle) to about 25 km/lp at the end of the sequence (lowest phase angle). Details are given in Table 1.

Initial processing of these images was the same as that outlined in Pollack *et al.* (1987), and included removal of blemishes and reseaux, dark current subtraction, and conversion (via a non-linear response function specific to each pixel) from DN value (0-255) to specific intensity (I/F) at each pixel. The precise pointing of each image was initially determined by fitting Triton's observed limb in the image to a circle of radius 1350 km, using the NAV program in the VICAR image handling package. Later the pointing was improved by comparing specific intensity profiles calculated from the best fitting atmospheric models to the observed I/F scans and determining whether all the limb scans for a given image could be better fit by shifting the observed limb.

Specific intensity was measured as a function of line-of-sight radius at intervals of approximately one pixel along selected radial lines crossing the limb of each image. The scan lines for all the images are shown projected onto the surface of Triton in Figure 1. As can be seen in this figure, the scan lines were chosen to correspond to ten distinct areas along the limb. The numerical analysis described in the following sections was carried out by using all the scans comprising a particular region to form a single data set covering a range of solar phase angles and wavelengths.

Before fitting the limb scans to the atmospheric models a final background subtraction was carried out by fitting a quadratic function to the portions of each limb scan well above the limb and well inside the terminator. This is necessary at high phase angles because some sunlight is scattered from the sunshade into the camera, and this is not included in the standard dark current sub-

traction. Also, the dark current is proportional to the temperature, and it is generally not possible to find a dark current frame taken at the same temperature as a given image.

3. Low latitudes (haze only)

The specific intensity as a function of radius was calculated for an atmosphere consisting of concentric homogeneous spherical shells using methods described in Rages and Pollack (1983) and Pollack *et al.* (1987). The spatial resolution of the high phase angle Triton images was not high enough to obtain meaningful vertical extinction profiles by directly inverting the radial intensity profiles. Instead, the radial intensity profiles were fit to simple exponential models of the extinction as a function of altitude.

At latitudes near the equator the atmospheric model contained a single component (haze), with a number density varying exponentially with altitude. The single scattering properties of the haze were described by Mie theory, with a complex refractive index and particle size that did not vary with altitude. The real part of the haze refractive index was assumed to be 1.285, consistent with the value for methane ice. The imaginary part of the refractive index was assumed to be a linear function of wavelength, $n_i = a + b\lambda$. The particle sizes were distributed according to a fairly narrow (width parameter 0.05) Hansen-Hovenier size distribution with a cross section weighted mean radius r_h.

It was assumed that there were no horizontal variations in the atmospheric properties over the entire area covered by the limb scans in any one region. This is a reasonably good assumption at low latitudes, but some of the higher latitude regions cover more than 30° of latitude, and in some cases (discussed in more detail in section 5.2) this assumption is clearly violated.

Triton's surface photometric properties were described by a single Hapke photometric function for each filter, with parameters given by Hillier *et al.* (1991) for the violet, blue, and green filters. Orange filter parameters were estimated by extrapolating from blue and green.

Specific intensities were calculated at 30-50 points along each radial scan at ten wavelengths between 0.3 μm and 0.65 μm, then convolved over both the various filter response functions (Danielson *et al.* 1981) and the point spread function (S.A. Collins, private communication) of the Voyager camera.

The haze column number density n_h, scale height H_h, mean particle radius r_h, and wavelength-dependent imaginary part of the refractive index were treated as free parameters in a least squares fitting procedure.

Results are shown in Figure 2 for a region near 15°S, 275°E (region 10). Three separate scattering models were found which gave acceptable fits to the imaging data: Rayleigh scattering, conservatively scattering particles with a mean radius of 0.19 μm, and 0.18 μm particles with an imaginary index which is moderately large in the violet and decreases toward longer wavelengths. The details of these three models can be found in Table 2, together with χ^2 divided by the number of degrees of freedom in each data set. The (radial) scattering optical depths for these models generally lie between 0.001 and 0.01 in all four filters, as shown in Table 3.

The Rayleigh scattering model fits the imaging data somewhat less well than the other two, and can be eliminated entirely by a comparison with data from the Voyager Ultraviolet Spectrometer (see Krasnopolsky *et al.* 1992). The Rayleigh scattering model predicts ultraviolet (slant) optical depths to the surface of around 10, which is an order of magnitude larger than those seen by the UVS. The other two models predict UV optical depths of about 0.15 if the imaginary index in the UV is given by extrapolating the linear function used in the visible. In fact, photochemically produced hydrocarbons could well have an absorption edge between 0.3 μm and 0.165 μm (the long wavelength limit of the UVS data) which could raise the UV optical depths to the 0.5-1.0 range observed.

The data from regions 1 and 9 were also fit to single component scattering models, and the details of these models are also given in Table 2. In both cases the derived imaginary index is very steeply sloping (in one case rising and in the other falling toward the red).

4. High latitudes (haze + cloud)

In light of the findings of Pollack *et al.* (1990) that both the haze and optically thicker discrete clouds can be present south of about 30°S, at these latitudes a two component model was fit to the data. This model contained the 0.19 μm conservatively scattering haze above an altitude of 8 km, with the column number density n_h and scale height H_h left as free parameters. Below 8 km there was another scattering component (cloud), with an independent exponential altitude profile defined by n_c and H_c, particle radius r_c, and wavelength dependent imaginary part of the refractive index. The real part of the cloud refractive index was taken to be 1.25, consistent with measured values for nitrogen ice (Thompson *et al.* 1973).

This model was applied to all the regions shown in Figure 1 except region 10. It soon became clear that large cloud optical depths (~1) were favored by the fitting algorithm. Optical depths this large are excluded by the images taken at lower phase angles and higher spatial resolutions, which show little or no indication of surface obscuration. Therefore an additional constraint was included in the fitting algorithm, specifying an upper bound τ_l on the total atmospheric optical depth. The function to be minimized was then

$$\chi^2 = \sum_{n=1}^{N} \frac{(I/F_c - I/F_o)_n^2}{\sigma_{on}^2} + \sum_{i=\mathrm{V,B,G,O}} f(\tau_i)^2 \qquad (1)$$

where the first summation is the usual formulation of χ^2 as the weighted sum over all N data points of the squares of the differences between the observed and calculated values of the dependent variable (in this case specific intensity), and

$$f(\tau_i) = 0 \qquad \tau_i < \tau_l$$
$$= \frac{(\tau_i - \tau_l)}{\sigma_\tau} \qquad \tau_i > \tau_l \qquad (2)$$

where σ_τ controls the "hardness" of the upper bound. Initially τ_l was set to 0.3 and σ_τ was set to 0.05.

Results for a typical high latitude region (region 3, near 50°S, 124°E) are shown in Figure 3. There are two distinct scattering models which fit the data for this region almost equally well. One contains cloud particles with a mean radius of 1.5 μm (solid line), while for the other this quantity is 0.22 μm (chain dotted line). Figure 4 illustrates how these two very different particle sizes could both fit the observations. It shows the albedo-weighted single scattering phase function for both models and all four filters. Although the larger particles have a much larger diffraction peak than the smaller particles, it is confined to scattering angles less than 20° (phase angles >160°), outside the limits of the Voyager observations. Between 20° and 40° scattering angle, the range which is covered by the observations, the two sets of phase functions are very similar.

The effect of lowering the atmospheric optical depth on the fit to the data was found by changing τ_l and σ_τ to 0.08 and 0.02 respectively, which limited the optical depth to around 0.1. The result is shown as the dashed line in Figure 3. Forcing the optical depth to be this low in this region increases χ^2 by a factor of 5.

The cloud scale height is more than 16 km, making the total thickness of the cloud layer less than half a scale height. It was not possible to determine whether the cloud was uniformly mixed with the gas, which has a scale height of around 18 km (Tyler *et al.* 1989), or whether the cloud mixing ratio increased with altitude as might be the case if condensation were occuring at the top of the cloud layer.

The best fitting parameter values for each two-component model studied for all of the regions 1-9 are given in Table 4. The total (vertical) optical depths for all the models (both one- and two-component) are given in Table 3. Most of the high latitude regions were similar to region 3 in

having two distinct particle size regimes that fit the data almost equally well. At the highest latitudes (regions 5, 6, and 7) r_m was near 0.7 μm or 0.3 μm. Region 9 was greatly affected by horizontal inhomgeneities in the atmospheric scatterers (see next section). Haze column number densities at high latitudes are about the same as they are at low latitudes (although at high latitudes the haze optical depth is given for 8 km altitude, while at low latitudes it is given at the surface). The two regions for which both one- and two-component models were tried (regions 1 and 9) the two-component models give significantly better fits to the observations.

5. Horizontal inhomogeneities

Many regions (especially those east of 180° longitude) showed features in the radial intensity profiles that can only be due to local variation in the atmospheric scattering properties. Figure 5 shows the complete data set from region 6, near 70°S, 175°E. In this region, most of the limb scans show a pronounced hump on the portion of the curve inside Triton's limb (radius less than 1350 km), represented by open circles in Figure 5. The surface is not bright enough in the scattering geometries represented by these scans for these humps to be due to variations in the surface properties, and this behavior cannot be produced by any extinction profile composed of homogeneous spherical shells. The most likely cause of the humps in this data set is a local increase in the cloud optical depth over part of the area covered by region 6. This is a strong indication that the "background" cloud optical depth in this region must be considerably less than unity.

The data points shown as open circles in Figure 5, and similar data points in the other regions, were not included in the data set used to define the values of the free parameters given in Table 4, because the two-component atmospheric model itself is inadequate for reproducing them. The location of all such data points are shown in Figure 6.

The most pronounced local variations in Triton's atmospheric scatterers seem to be concentrated in a diagonal band between 55° and 15° south latitude, and 180° and 270° east longitude. A comparison of Figure 6 with Figure 1 shows that this apparent concentration is not merely a se-

lection effect. The part of Triton covered by the high phase angle images is (more or less inevitably) on the opposite side of the satellite from the region covered at the highest spatial resolution at lower phase angles. Therefore the characteristics of the surface in the band of local atmospheric variability are known only vaguely. According to McEwen (1990), this band lies mostly over the bright south polar cap, with its northern end extending into the brighter polar cap fringe. The band of pronounced atmospheric variability lies along the evening terminator, so it could be an indicator of some kind of diurnal effect.

The plumes visible on the highest resolution images of Triton, marked by ×'s in Figure 6, are also in the opposite hemisphere from the areas of local variability seen at high phase angles. One area which Pollack *et al.* (1990) noted as unusual because it lacked the otherwise ubiquitous haze is somewhat closer to the variable regions (dashed ellipse in Figure 6).

6. Discussion

Sagan and Chyba (1990) give an expression for the sedimentation velocity of particles in Triton's atmosphere as a function of particle size. Assuming a surface pressure of 12 μbar, and an "equivalent isothermal temperature" of 48K (from Tyler *et al.* 1989) to characterize the variation of pressure with altitude, this expression gives fall times to the surface from an altitude of 8 km of order 1 day for 1.5 μm particles and 1 week for 0.23 μm particles.

Using the coagulation kernal given by Turco *et al.* (1982), simplified by assuming monodesperse particle sizes, coagulation times are found to be of order 1 month for small cloud particles and 1 year for large ones. Condensation times are critically dependent on the difference between ambient pressure and the saturation vapor pressure, neither of which is known well enough to yield useful limits.

The fact that the coagulation times are substantially longer than the fallout times may constitute further evidence that condensation is taking place, but it is not possible to discriminate between the two possible cloud particle size regimes by comparing growth and fallout times.

Nitrogen is the major constituent of Triton's atmosphere, and its ambient pressure is essentially the same everywhere on Triton. If the clouds are composed of condensed N_2, the fact that they appear preferentially toward the south pole would indicate systematically lower atmospheric temperatures there, despite the fact that solar insolation is currently highest at high southern latitudes. Spencer and Moore (1992) have postulated that the high southern latitudes of Triton may be mostly frost free, with the high surface albedo produced by a non-volatile substrate such as H_2O or CO_2 ice, and at least some of their frost-free models have surface temperatures which decrease monotonically between the equator and 60-70°S. To the extent that surface temperatures on Triton can be correlated with atmospheric temperatures, this would be consistent with increased N_2 condensation at higher southern latitudes.

References

CRUIKSHANK, D.P., R.H. BROWN, AND R.N. CLARK 1984. Nitrogen on Triton. *Icarus* **58,** 293-305.

CRUIKSHANK, D.P., R.H. BROWN, L.P. GIVER, AND A.T. TOKUNAGA 1989. Triton: Do we see the surface?. *Science* **245,** 283-286.

DANIELSON, G.E., P.N. KUPFERMAN, T.V. JOHNSON, AND L.A. SODERBLOM 1981. Radiometric performance of the Voyager cameras. *J. Geophys. Res.* **86,** 8683-8689.

HILLIER, J.K., P. HELFENSTEIN, A. VERBISCER, AND J. VEVERKA 1991. Voyager photometry of Triton: Haze and surface photometric properties. *J. Geophys. Res.* **96,** 19,203-19,209.

KRASNOPOLSKY, V.A., B.R. SANDEL, AND F. HERBERT 1992. Properties of haze in the atmosphere of Triton. *Neptune and Triton Conference Proceedings,* Tucson, Arizona, January 1992, pp. 39.

MCEWEN, A.S. 1990. Global color and albedo variations on Triton. *Geophys. Res. Lett.* **17,** 1765-1768.

POLLACK, J.B., K. RAGES, S.K. POPE, M.G. TOMASKO, P.N. ROMANI, AND S.K. ATREYA 1987. Nature of the stratospheric haze on Uranus: Evidence for condensed hydrocarbons. *J. Geophys. Res.* **92,** 15,037-15,065.

POLLACK, J.B., J.M. SCHWARTZ, AND K. RAGES 1990. Scatterers in Triton's atmosphere: Implications for the seasonal volatile cycle. *Science* **250,** 440-443.

RAGES, K., AND J.B. POLLACK 1983. Vertical distribution of scattering hazes in Titan's upper atmosphere. *Icarus* **55,** 50-62.

SAGAN, C., AND C. CHYBA 1990. Triton's streaks as windblown dust. *Nature* **346,** 546-548.

SMITH, B.A., L.A. SODERBLOM, D. BANFIELD, C. BARNET, A.T. BASILEVSKY, R.F. BEEBE, K. BOLLINGER, J.M. BOYCE, A. BRAHIC, G.A. BRIGGS, R.H. BROWN, C. CHYBA, S.A.

COLLINS, T. COLVIN, A.F. COOK II, D. CRISP, S.K. CROFT, D. CRUIKSHANK, J.N. CUZZI, G.E. DANIELSON, M.E. DAVIES, E. DE JONG, L. DONES, D. GODFREY, J. GOGUEN, I. GRENIER, V.R. HAEMMERLE, H. HAMMEL, C.J. HANSEN, C.P. HELFENSTEIN, C. HOWELL, G.E. HUNT, A.P. INGERSOLL, T.V. JOHNSON, J. KARGEL, R. KIRK, D.I. KUEHN, S. LIMAYE, H. MASURSKY, A. MCEWEN, D. MORRISON, T. OWEN, W. OWEN, J.B. POLLACK, C.C. PORCO, K. RAGES, P. ROGERS, D. RUDY, C. SAGAN, J. SCHWARTZ, E.M. SHOEMAKER, M. SHOWALTER, B. SICARDY, D. SIMONELLI, J. SPENCER, L.A. SROMOVSKY, C. STOKER, R.G. STROM, V.E. SUOMI, S. P. SYNOTT, R.J. TERRILE,P. THOMAS, W.R. THOMPSON, A. VERBISCER, AND J. VEVERKA 1989. Voyager 2 at Neptune: Imaging science results. *Science* **246,** 1422-1449.

SPENCER, J.R., AND J.M. MOORE 1992. The influence of thermal inertia on temperatures and frost stabillity on Triton. *Icarus*, in press..

THOMPSON, S.B., F. ARNOLD, R.B. SANDERSON, AND A.W. MANTZ 1973. Optical properties of cryodeposits on low scatter mirrors. *AIAA 8th Thermophysics Conference Proceedings,* Palm Springs, California, July 16-18 1973.

TURCO, R.P., O.B. TOON, R.C. WHITTEN, R.G. KEESEE, AND D. HOLLENBACH 1982. Noctilucent clouds: Simulation studies of their genesis, properties and global influences. *Planet. Space Sci.* **30,** 1147-1181.

TYLER, G.L., D.N. SWEETNAM, J.D. ANDERSON, S.E. BORUTZKI, J.K. CAMPBELL, V.R. ESHLEMAN, D.L. GRESH, E.M. GURROLA, D.P. HINSON, N. KAWASHIMA, E.R. KURSINSKI, G.S. LEVY, G.F. LINDAL, J.R. LYONS, E.A. MAROUF, P.A. ROSEN, R.A. SIMPSON, AND G.E. WOOD 1989. Voyager radio science observations of Neptune and Triton. *Science* **246,** 1466-1473.

Table 1: Description of Triton Images

FDS count	Camera and Filter	Phase angle (°)	Resolution (km/lp)
11398.11	WA-B	159.2	9.5
11398.17	WA-G	157.8	10.1
11398.23	WA-V	156.4	10.6
11398.29	WA-B	155.0	11.2
11398.35	WA-G	153.5	11.7
11398.56	WA-V	150.2	12.7
11399.07	WA-G	148.0	14.8
11399.18	WA-B	148.0	15.9
11399.29	WA-O	146.1	17.0
11399.51	WA-B	144.5	19.1
11400.02	WA-G	143.9	20.2
11400.13	WA-V	143.8	21.4
11400.24	WA-B	143.8	22.4
11400.48	WA-O	141.3	24.8
11400.54	WA-G	141.3	25.4

Table 2: Optimum Values of Free Parameters for 1-Component Models

Region	model	r_h (μm)	n_h (10^8 cm^{-2})	H_h (km)	a	b (μm^{-1})	χ^2 /d.o.f.
1	a)	0.162±0.007	0.22±0.05	5.4±0.3	–0.5±0.4	1.6±0.8	0.80
9	a)	0.0962±0.0012	3.4±0.5	5.1±0.3	1.1±0.3	–1.6±0.4	1.28
10	a)	0.182±0.017	0.037±0.018	10.8±0.7	0.12±0.15	–0.2±0.4	0.79
	b)	0.188±0.014	0.029±0.010	11.0±0.6	0.0	0.0	0.80
	c)	0.025	3720±140	10.8±0.6	0.0	0.0	0.92

Table 3: Model Optical Depths

		Vertical optical depth to surface			
Region	model	Violet	Blue	Green	Orange
1	a)	0.027	0.028	0.031	0.032
	b)	0.127	0.126	0.125	0.125
	c)	0.039	0.040	0.042	0.041
2	a)	0.309	0.307	0.304	0.308
	b)	0.364	0.319	0.237	0.208
	c)	0.111	0.100	0.082	0.076
3	a)	0.364	0.360	0.357	0.361
	b)	0.409	0.353	0.254	0.221
	c)	0.117	0.104	0.084	0.078
4	a)	0.369	0.364	0.361	0.366
	b)	0.411	0.355	0.255	0.221
	c)	0.121	0.104	0.077	0.068
5	a)	0.351	0.358	0.352	0.345
	b)	0.374	0.346	0.294	0.276
	c)	0.112	0.102	0.086	0.080
6	a)	0.362	0.355	0.328	0.317
	b)	0.360	0.345	0.328	0.324
	c)	0.105	0.100	0.100	0.101
7	a)	0.358	0.358	0.342	0.333
	b)	0.377	0.356	0.314	0.298
	c)	0.109	0.103	0.095	0.093
8	a)	0.343	0.344	0.343	0.342
	b)	0.386	0.323	0.188	0.136
	c)	0.097	0.096	0.093	0.091
9	a)	0.143	0.117	0.065	0.046
	b)	0.151	0.151	0.151	0.152
	c)	0.331	0.266	0.164	0.134
	d)	0.089	0.089	0.087	0.084
10	a)	0.0047	0.0039	0.0024	0.0020
	b)	0.0036	0.0030	0.0020	0.0017
	c)	0.0143	0.0100	0.0050	0.0039

Table 4: Optimum Values of Free Parameters for 2-Component Models

Region	Model	r_m (μm)	n_c (10^6cm^{-2})	H_c (km)	n_h (10^6 cm^{-2})	H_h (km)	a	b (μm^{-1})	χ^2 /d.o.f.
1	b)	1.70±0.14	0.6±0.2	1.0±0.2	2.73±0.14	7.1±0.5	–0.015±0.009	0.06±0.02	0.53
	c)	0.168±0.007	25±6	2.0±0.2	2.38±0.11	7.7±0.5	–0.41±0.14	1.6	0.59
2	a)	1.50±0.08	1.9±0.6	16±29	3.3±0.3	10.4±0.9	–0.031±0.004	0.08±0.01	1.19
	b)	0.211±0.006	176±20	8±3	3.1±0.3	11.2±1.1	0.18±0.02	–0.19±0.04	1.35
	c)	0.205±0.012	59±12	16±19	1.7±0.4	14±4	0.05±0.06	0.09±0.12	4.71
3	a)	1.48±0.07	2.3±0.2	16±9	4.2±0.3	9.5±0.8	–0.025±0.003	0.059±0.007	1.56
	b)	0.219±0.005	184±15	16±9	4.2±0.4	9.9±0.9	0.157±0.016	–0.20±0.03	1.69
	c)	0.201±0.011	74±16	16±21	1.5±0.6	14±6	0.00±0.05	0.11±0.10	8.21
4	a)	1.46±0.06	2.4±0.2	16±12	5.9±0.4	8.9±0.7	–0.027±0.003	0.063±0.006	1.95
	b)	0.223±0.004	175±13	16±11	6.1±0.5	9.1±0.7	0.138±0.014	–0.17±0.03	2.04
	c)	0.215±0.010	63±11	16±21	2.1±0.7	14±5	0.05±0.03	–0.02±0.07	8.85
5	a)	0.716±0.012	7.4±0.4	16±14	7.3±0.4	9.2±0.5	–0.05±0.01	0.17±0.02	1.27
	b)	0.270±0.004	83±5	16±13	8.6±0.5	8.7±0.5	0.14±0.04	–0.02±0.07	1.29
	c)	0.264±0.008	27±3	16±21	5.0±0.7	11.0±1.5	0.02±0.06	0.13±0.12	4.28
6	a)	0.663±0.009	8.6±0.4	16±14	7.1±0.3	9.1±0.5	–0.124±0.015	0.35±0.04	1.25
	b)	0.297±0.004	61±4	16±14	8.5±0.4	8.5±0.4	–0.20±0.08	0.76±0.17	1.29
	c)	0.298±0.008	17.2±1.4	16±22	6.0±0.7	9.8±1.1	–0.61±0.16	1.6±0.4	3.80
7	a)	0.690±0.011	8.2±0.4	16±16	7.2±0.4	9.7±0.6	–0.075±0.014	0.25±0.03	1.78
	b)	0.271±0.004	79±5	16±15	8.7±0.5	9.2±0.5	0.22±0.08	–0.06±0.15	1.69
	c)	0.276±0.008	22.0±1.9	16±23	5.5±0.7	11.1±1.4	–0.09±0.12	0.5±0.2	4.67
8	a)	1.79±0.08	1.49±0.15	16±23	5.3±0.3	9.3±0.6	–0.036±0.008	0.111±0.019	1.55
	b)	0.153±0.004	330±60	16±19	5.7±0.3	9.4±0.6	0.8±0.2	–1.2±0.4	1.45
	c)	0.174±0.006	50±4	16±26	4.3±0.5	10.6±1.2	0.1±0.4	0.8±0.9	2.67
9	b)	2.019±0.004	0.52±0.04	16±24	2.38±0.15	11.7±1.0	–0.085±0.013	0.25±0.03	0.79
	c)	0.08±0.02	3600±5000	16±21	2.67±0.14	11.4±0.8	0.18±0.17	–0.2±0.2	0.57
	d)	0.100±0.003	203±14	16±24	2.54±0.16	11.2±0.9	–0.0±0.3	1.0±0.6	0.72

Figure captions

1. This figure shows the locations of the data sets fit to the spherical shell atmospheric models. The location of Triton's limb in each of the green filter images is shown by the heavy lines, with the corresponding FDS numbers given in the legend. Each sheaf of thinner curved lines perpendicular to the limbs represents the radial limb scans taken from each of the 15 images, for each of ten labelled regions. These labels correspond to the region numbers in Tables 2, 3, and 4. Finally, the location of the surface terminator is shown (thin solid line), as well as the location where the sun drops below the horizon for an altitude of 10 km above the surface (thin dashed line). Note that for some regions the limb scans cover more than 30° in latitude, which makes it rather unlikely that the atmosphere is homogeneous throughout the region.

2. This is the complete data set for region 10, shown together with three possible model atmospheres: conservative scatterers with a mean particle radius of 0.19 μm (solid line), highly absorbing particles with a mean radius of 0.18 μm (chain-dotted line), and Rayleigh scatterers (dashed line).

3. This is the complete data set for region 3. Three model atmospheres are shown: a) ≈0.3 optical depths of 1.5 μm particles (solid line), b) ≈0.3 optical depths of 0.22 μm particles (chain dotted line), and c) ≈0.1 optical depths of 0.20 μm particles (dashed line). Model c) fits the data much less well than the other two.

4. Albedo weighted single scattering phase function between 0° and 50° scattering angle, for models a) (solid line) and b) (dashed line) from Figure 3.

5. This is the complete data set for region 6. This is an example of an "ill behaved'' region, since many of the limb scans contain humps at radii less that 1350 km, which cannot possibly be fit by any horizontally homogeneous atmosphere, even if the condition of an exponential extinction profile is relaxed. The points shown as open circles were not included in the least-squares fitting procedure.

6. The location of all the points in all the radial scans for which I/F was clearly affected by local inhomogeneities (most likely local increases in the optical depth) in the cloud properties. The size of each dot crudely corresponds to the amount by which I/F deviated from its "background" value. The size of two plumes seen in the highest resolution images of the surface are marked by ×'s, and the location of a haze free area noted by Pollack *et al.* (1990) is shown as a dashed ellipsoid.

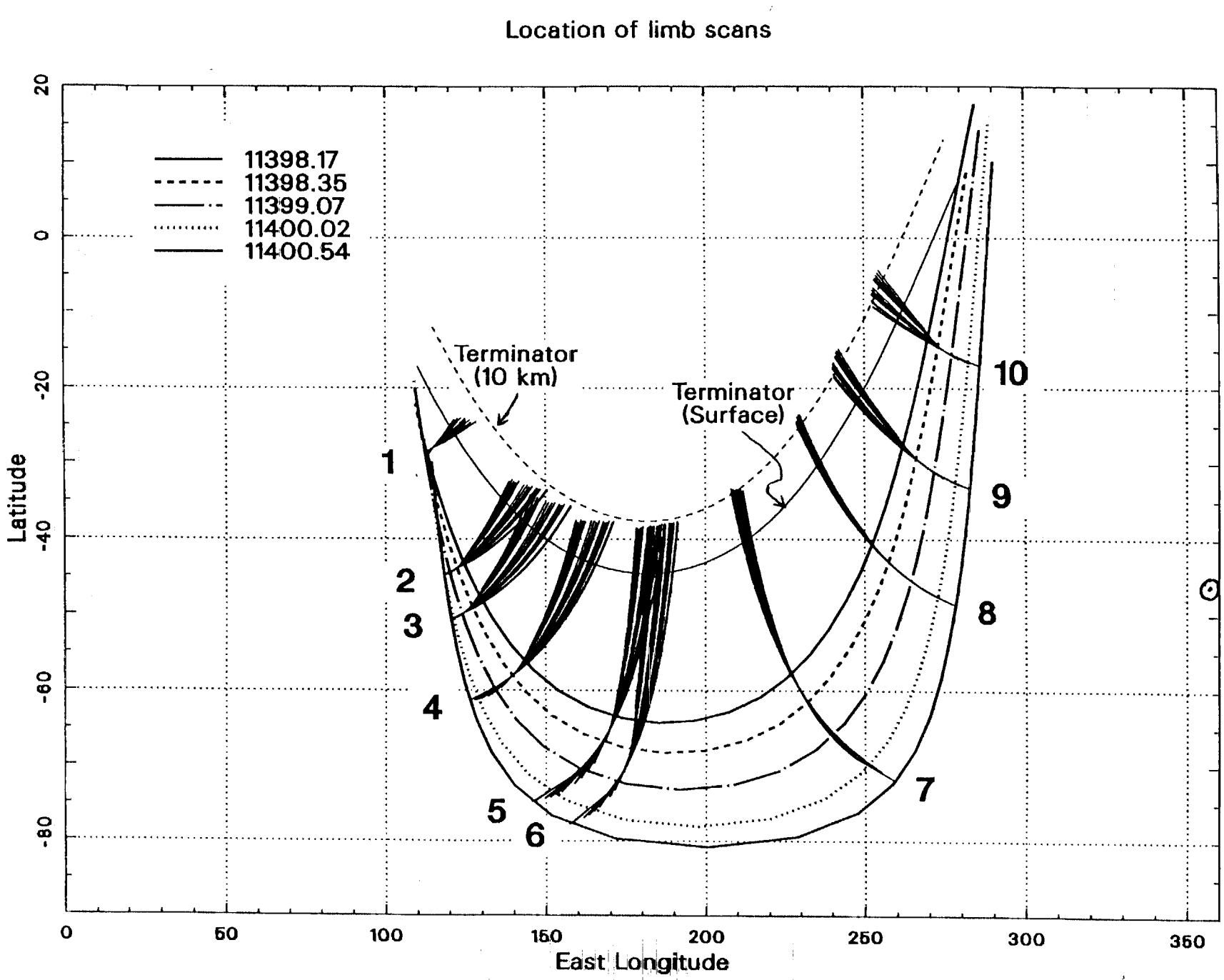
Location of limb scans
11398.17
11398.35
11399.07
11400.02
11400.54
Terminator
(10 km)
Terminator
(Surface)
1
2
3
4
5
6
7
8
9
10
Latitude
East Longitude
20
0
-20
-40
-60
-80
0
50
100
150
200
250
300
350

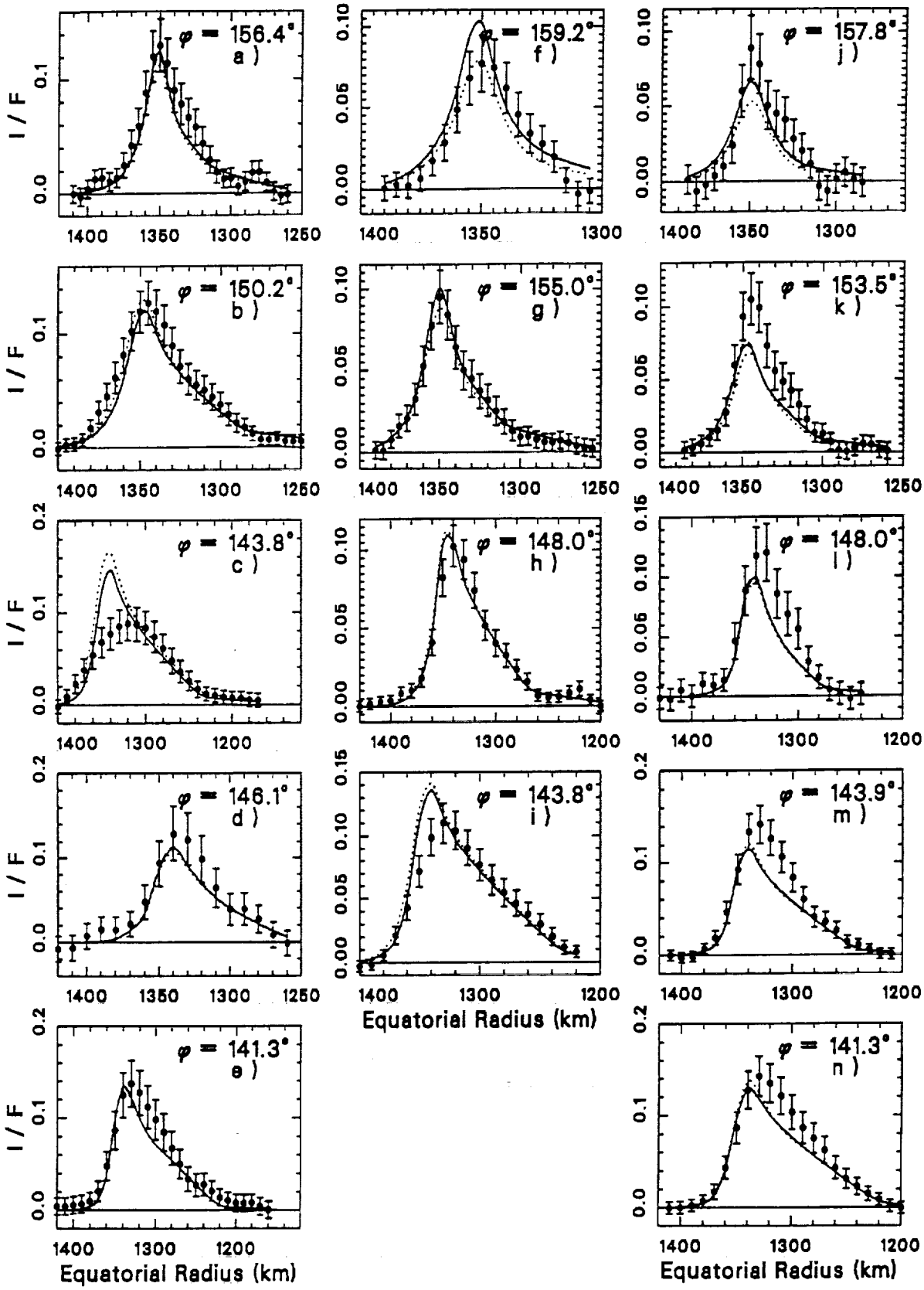
φ = 156.4° a)
φ = 159.2° f)
φ = 157.8° j)
φ = 150.2° b)
φ = 155.0° g)
φ = 153.5° k)
φ = 143.8° c)
φ = 148.0° h)
φ = 148.0° l)
φ = 146.1° d)
φ = 143.8° i)
φ = 143.9° m)
φ = 141.3° e)
φ = 141.3° n)
I / F
Equatorial Radius (km)

Fig. 2

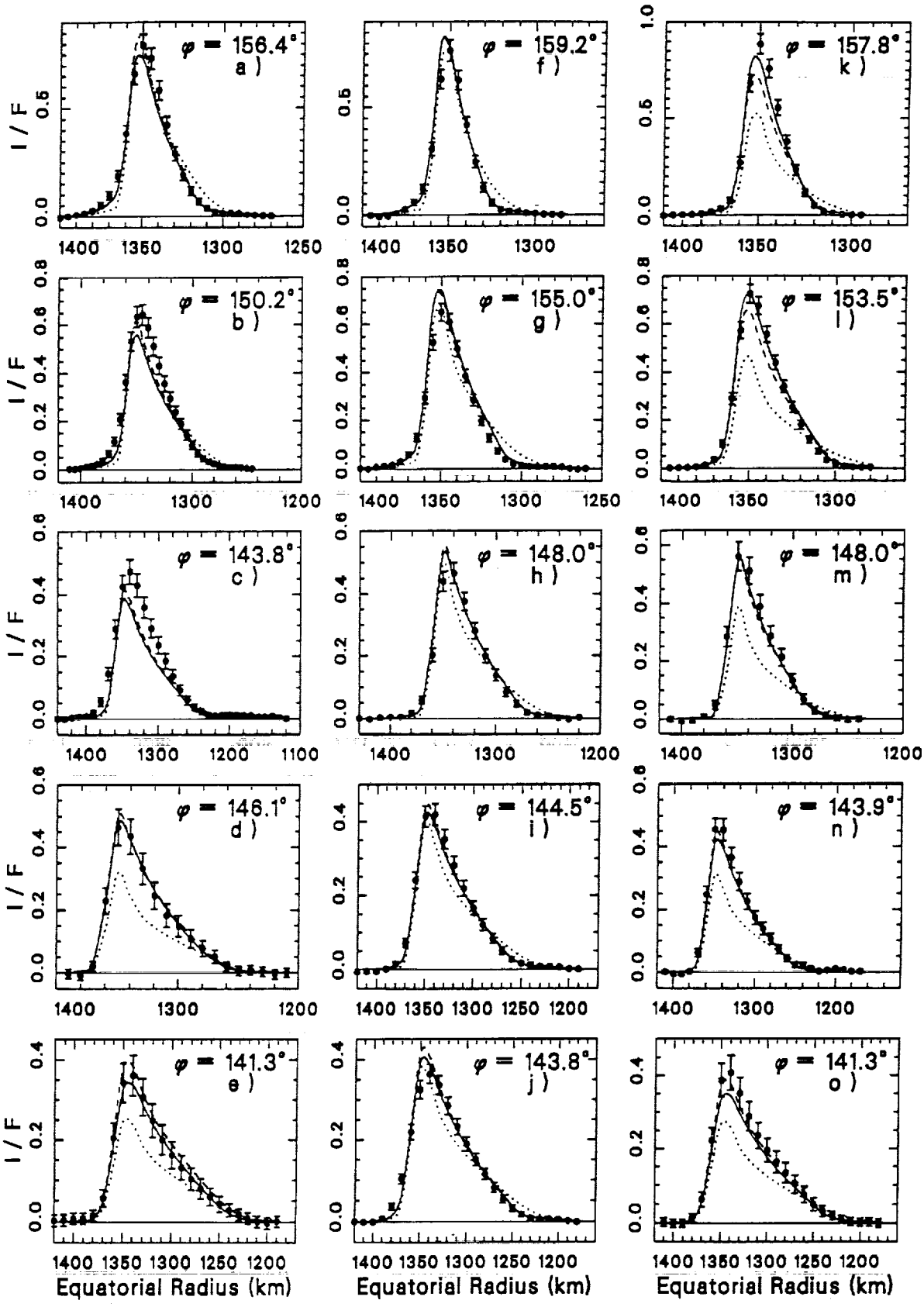
φ = 156.4° a)
φ = 159.2° f)
φ = 157.8° k)
φ = 150.2° b)
φ = 155.0° g)
φ = 153.5° l)
φ = 143.8° c)
φ = 148.0° h)
φ = 148.0° m)
φ = 146.1° d)
φ = 144.5° i)
φ = 143.9° n)
φ = 141.3° e)
φ = 143.8° j)
φ = 141.3° o)
I / F
Equatorial Radius (km)

Fig. 3

Triton Phase Function -- 50°S Latitude

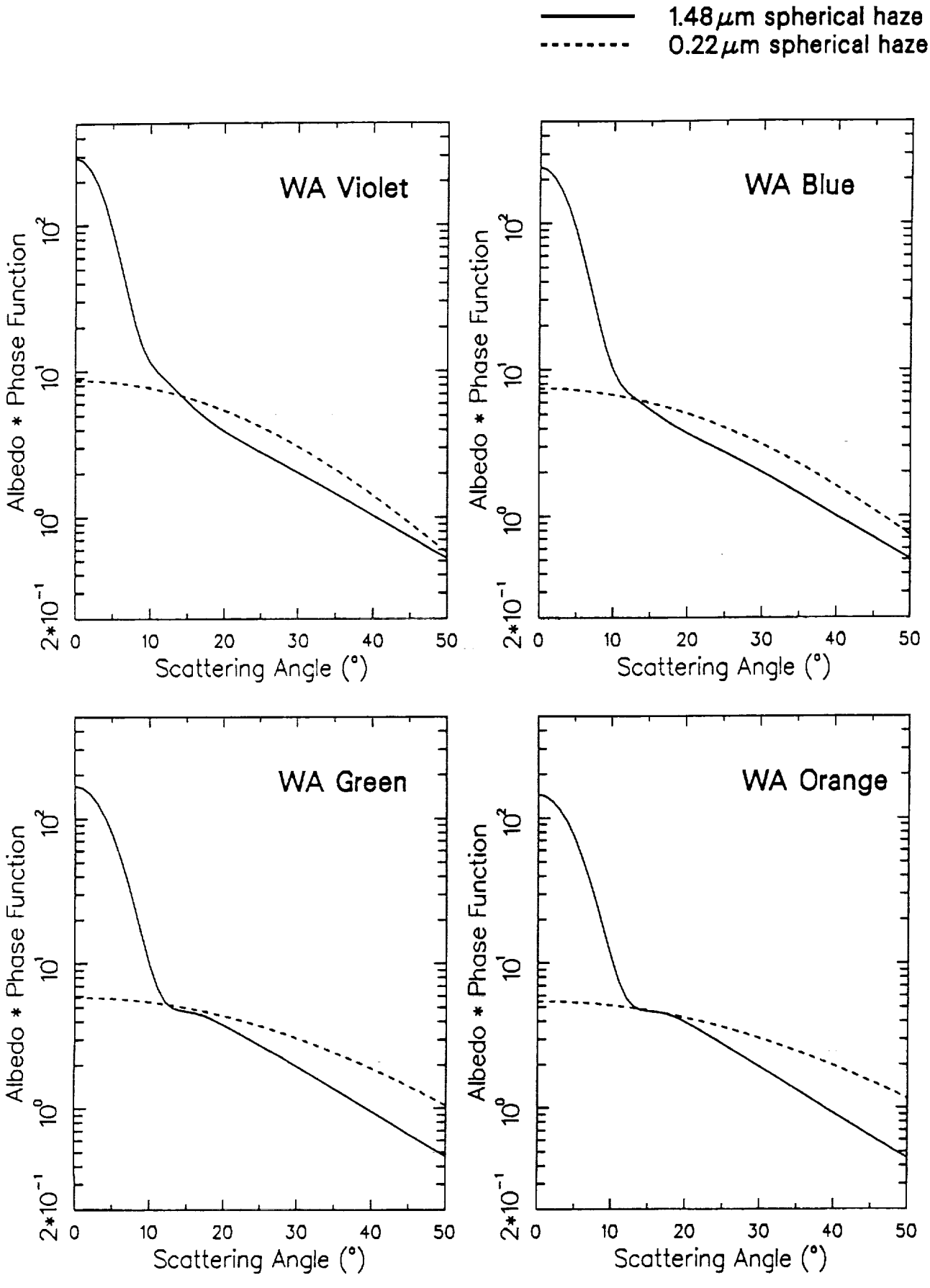

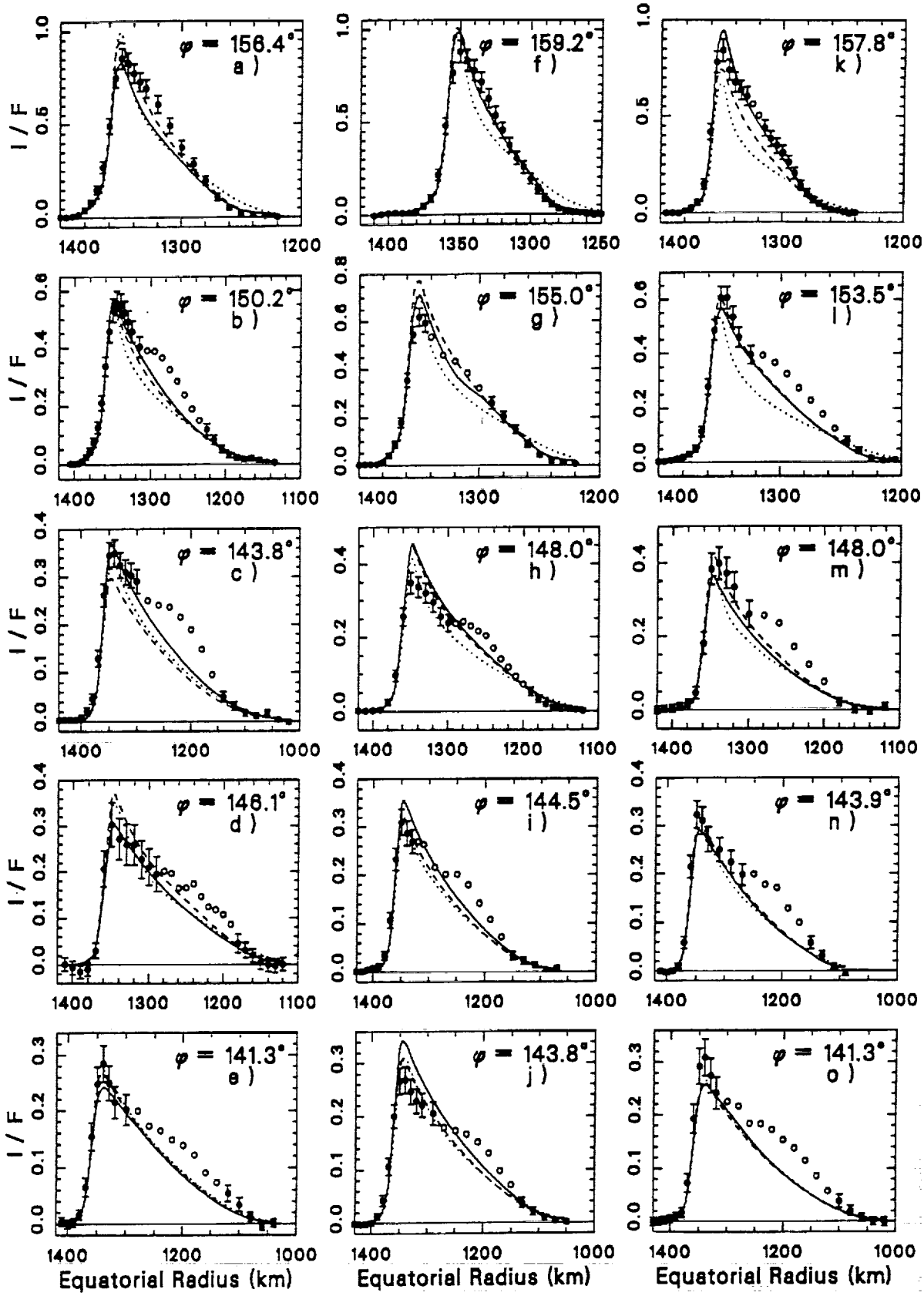
I / F
φ = 156.4°
a)
φ = 159.2°
f)
φ = 157.8°
k)
φ = 150.2°
b)
φ = 155.0°
g)
φ = 153.5°
l)
φ = 143.8°
c)
φ = 148.0°
h)
φ = 148.0°
m)
φ = 146.1°
d)
φ = 144.5°
i)
φ = 143.9°
n)
φ = 141.3°
e)
φ = 143.8°
j)
φ = 141.3°
o)
Equatorial Radius (km)
Equatorial Radius (km)
Equatorial Radius (km)

Fig. 5

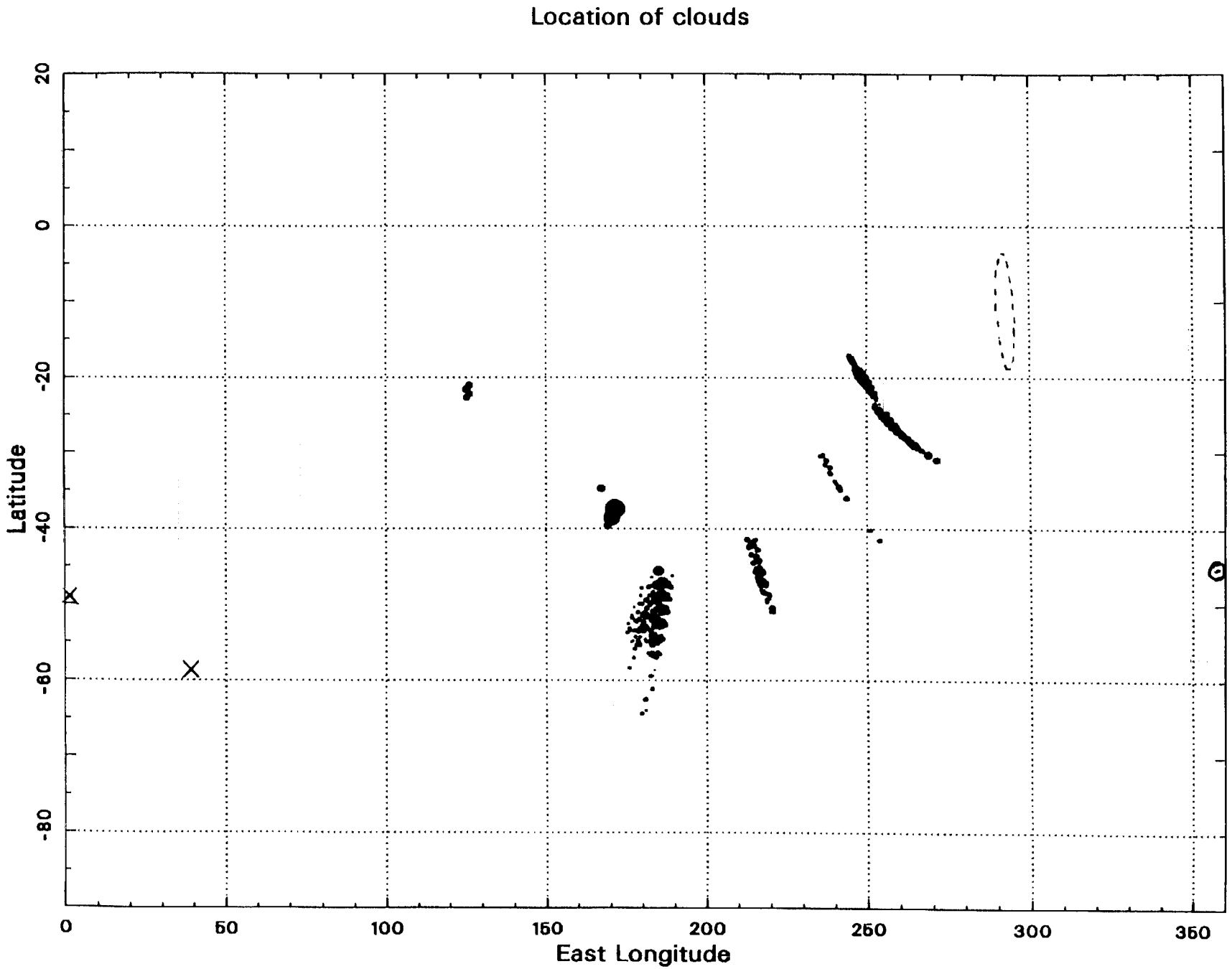
Location of clouds
Latitude
East Longitude
20
0
-20
-40
-60
-80
0
50
100
150
200
250
300
350